Physics and Chemistry of Minerals (2021) 48:35
https://doi.org/10.1007/s00269-021-01157-3

ORIGINAL PAPER

Dislocation structure of deformed olivine single crystals from conventional EBSD maps

Ulrich Faul[1,2]

Received: 16 April 2021 / Accepted: 28 July 2021 / Published online: 6 September 2021
© The Author(s) 2021

Abstract

Dislocations, linear defects in a crystalline lattice characterized by their slip systems, can provide a record of grain internal deformation. Comprehensive examination of this record has been limited by intrinsic limitations of the observational methods. Transmission electron microscopy reveals individual dislocations, but images only a few square µm of sample. Oxidative decoration requires involved sample preparation and has uncertainties in detection of all dislocations and their types. The possibility of mapping dislocation density and slip systems by conventional (Hough-transform based) EBSD is investigated here with naturally and experimentally deformed San Carlos olivine single crystals. Geometry and dislocation structures of crystals deformed in orientations designed to activate particular slip systems were previously analyzed by TEM and oxidative decoration. A curvature tensor is calculated from changes in orientation of the crystal lattice, which is inverted to calculate density of geometrically necessary dislocations with the Matlab Toolbox MTEX. Densities of individual dislocation types along with misorientation axes are compared to orientation change measured on the deformed crystals. After filtering (denoising), noise floor and calculated dislocation densities are comparable to those reported from high resolution EBSD mapping. For samples deformed in [110]c and [011]c orientations EBSD mapping confirms [100](010) and [001](010), respectively, as the dominant slip systems. EBSD mapping thus enables relatively efficient observation of dislocation structures associated with intracrystalline deformation, both distributed, and localized at sub-boundaries, over substantially larger areas than has previously been possible. This will enable mapping of dislocation structures in both naturally and experimentally deformed polycrystals, with potentially new insights into deformation processes in Earth's upper mantle.

Keywords Dislocations · Olivine · EBSD · Deformation · Mtex

Introduction

Observations from experimentally and naturally deformed olivine single and polycrystals show that olivine deforms by a limited number of slip systems in dislocation creep. The slip systems most commonly observed resulting from high temperature creep of olivine (1150–1600 °C for the experiments cited) are [100](010), [100](001), [001](100) and [001](010) [Durham and Goetze (1977), Darot and Gueguen (1981), Bai and Kohlstedt (1991), see also reviews by Tommasi et al. (2000), Cordier et al. (2014), Wallis et al. (2016)]. [100](010) and [001](010) are the softest and hardest slip systems, respectively, under dry, high temperature conditions (Hirth and Kohlstedt 2003). No glide loops are observed for dislocations with Burgers vector $\mathbf{b} = [010]$, corresponding to the longest dimension of the unit cell. Dislocations with this Burgers vector, therefore, do not contribute to crystal plastic strain in olivine (Durham et al. 1977; Gueguen and Darot 1982; Fujino et al. 1993; Cordier et al. 2014).

In these studies, dislocation structures were analyzed by oxidative decoration (Kohlstedt 1976) and transmission electron microscopy (TEM). Oxidative decoration requires the presence of Fe in the crystal, and needs significant additional sample preparation and analyses of images [e.g., Jaoul et al. (1979), Karato and Lee (1999)]. Obtaining accurate dislocation densities with this method is not entirely straight forward (Durham et al. 1977; Farla et al. 2011; Wallis et al. 2016). The area of observation is usually < 100 µm [e.g.,

✉ Ulrich Faul
hufaul@mit.edu

1 Geology Department, State University of New York at New Paltz, New York, USA

2 Massachusetts Institute of Technology, Cambridge, MA, USA

Toriumi and Karato (1979)], and it is not routinely used for post-experimental sample analysis of polycrystalline samples. TEM methods again require additional sample preparation, expertise and access to a TEM, but investigation of structures larger than a few µm is impractical (c.f. mm-sized samples).

High-resolution EBSD (HR-EBSD) enables acquisition of maps with substantially higher angular fidelity in comparison to conventional Hough transform based EBSD (Britton et al. 2010). This allows dislocation structures and densities to be extracted from EBSD maps (Wilkinson et al. 2006; Wilkinson and Randman 2010; Britton and Wilkinson 2012). Wallis et al. (2016, 2017a, b, 2019a, b) describe the use of HR-EBSD mapping to calculate dislocation structures and densities in deformed olivine single and polycrystals as well as natural quartz samples. While the angular resolution of conventional, Hough transform based EBSD mapping is not nearly as good as that of HR-EBSD, conventional EBSD is not nearly as computationally expensive and does not require specialized procedures or software. Cordier et al. (2014) show an example of the dislocation density tensor calculated from conventional EBSD data for an experimentally deformed polycrystalline olivine aggregate.

Durham et al. (1977) examined dislocation structures of single crystals deformed by Durham and Goetze (1977) by light microscopy imaging of decorated sections and TEM imaging. These observations provide a useful reference for comparison with observations from conventional EBSD mapping. Below conventional EBSD maps from two of their samples are used to examine dislocation structures in experimentally deformed single crystals of olivine.

Dislocation geometry

For interpretation of the dislocation densities observed in EBSD maps, it is useful to first consider geometrical aspects of dislocations. EBSD mapping detects changes in orientation of the crystal lattice, but does not image individual dislocations directly, in contrast to imaging of decorated sections or TEM imaging. On the other hand, it is not possible to quantify crystal lattice orientation changes due to dislocations from decorated sections as for example dislocations of opposite polarity can not be distinguished. Additionally, the orientation of the crystal has to be known to infer dislocation types.

The geometry of the edge dislocations considered here is illustrated in Fig. 1a [c.f. Wallis et al. (2017a)]. The cartoon shows distributed dislocations, as well as dislocations concentrated in a glide plane, denoted as slip band. The dislocation line for [100](010) edge dislocation, representing the termination of the extra half plane, is parallel to the [001] direction. For [100](010) edge dislocations, slip bands correspond therefore to on-end rows of dislocations in decorated sections in the (001) plane [e.g., Durham et al. (1977), Fig. 1a; Darot and Gueguen (1981) Fig. 7d]. For this dislocation type the [001] crystal axis is the axis of rotation for the angular change in the [100] direction, denoted below as misorientation axis. Correspondingly, the dislocation line

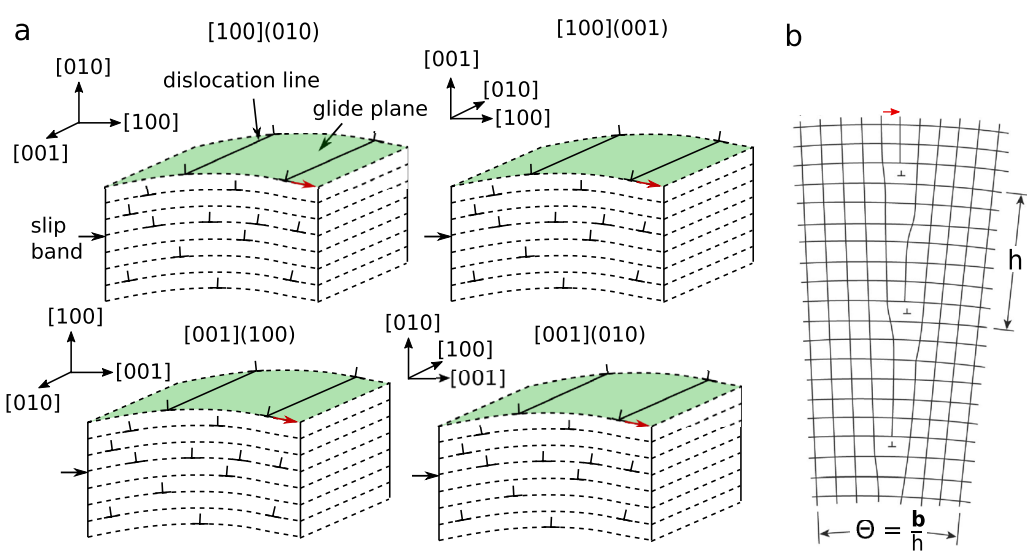

Fig. 1 **a** Illustration of Burgers vector (red arrows), glide plane, and change in orientation of a crystal lattice for the edge dislocations considered here. Rotation of the crystal lattice occurs around the dislocation line, referred to as the misorientation axis in the following. No change in orientation occurs parallel to the dislocation lines in a plane perpendicular to the Burgers vector (i.e., perpendicular to the glide plane) [after Wallis et al. (2017a)]. **b** Illustration of the change in orientation of the crystal lattice parallel to the direction of the Burgers vector. The angle θ is inversely related to the spacing of the dislocations (or dislocation density). Edge dislocations concentrated in a plane perpendicular to their Burgers vector form a tilt wall

directions for the other edge dislocations represent the misorientation axes for these dislocations.

[100](010) edge dislocations arranged in a plane perpendicular to [100] form a sub-boundary (tilt wall, Fig. 1b). The lattice curvature resulting from distributed dislocations (Fig. 1a) or sub-boundaries is inversely related to dislocation spacing or dislocation density in the glide plane [e.g., Poirier (1985)]. No change in orientation occurs in the plane perpendicular to the Burgers vector and glide plane of edge dislocations [see also Wallis et al. (2016)].

The dislocations in Fig. 1 have all the same polarity and therefore macroscopically change the orientation of the crystal lattice. They constitute geometrically necessary dislocations. Adjacent dislocations with opposite polarity at a distance less than a particular EBSD mapping stepsize cause no detectable lattice curvature. Dislocation structures not contributing to a net change in curvature are termed statistically stored dislocations [e.g., Kröner (1958)].

For the edge dislocations shown in Fig. 1, misorientation axes can only coincide with the crystallographic [100], [010], and [001] axes. For screw dislocations, with Burgers vector parallel to the dislocation line, arbitrary misorientation axes perpendicular to the Burgers vector are possible in principle, but are constrained by the atomic structure of the unit cell. The primary slip plane of screw dislocations is typically that of edge dislocations with the same Burgers vector.

Sample preparation

Two samples deformed by Durham and Goetze (1977) and an as received (naturally deformed) San Carlos olivine single crystal were mapped by EBSD and discussed below. Sample 7506-2 was deformed at 1600 °C to a strain of 29 % in the [110]c orientation, for which the compression direction bisects the angle between [100] and [010] (Fig. 2). In this orientation, the softest slip system for (dry) olivine, [100](010), has the greatest resolved shear stress (Table 1). The sample surface mapped here is the mirror image (underside) relative to that shown in Durham et al. (1977), Fig. 1a. Sample 7406-2 was deformed at 1600 and 1200 °C to a total strain of 21% in the [011]c orientation, designed to activate the hardest slip system in olivine, [001](010). Table 1 indicates that for both orientations the shear stress on the other glide systems was near 15% of that on the intended glide system due to slight misalignment of the crystals relative to the intended orientations.

Table 1 Schmid factors calculated for the four main high-temperature glide systems

Sample	Orientation	[100](010)	[100](001)	[001](100)	[001](010)
7406-2	[011]c	0.08	0.06	0.06	0.47
7506-2	[110]c	0.44	0.05	0.05	0.08

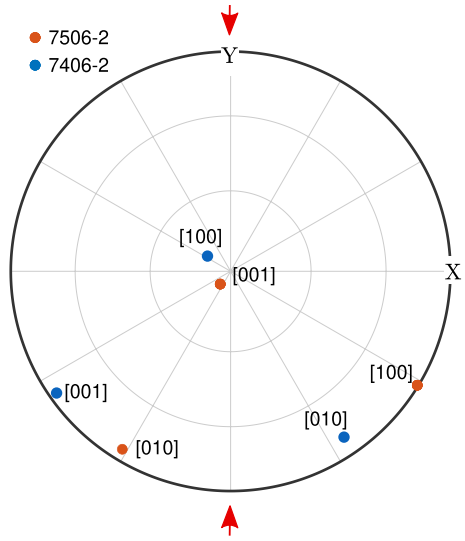

Fig. 2 Orientation of two single crystals deformed by Durham and Goetze (1977). 7506-2 was deformed in the [110]c orientation, 7406-2 in the [011]c orientation. Compression direction is shown by red arrows. This coordinate system applies to the EBSD maps shown below. Orientations represent the mean orientation of the maps with the larger stepsize; both crystals are deformed and have a range of orientations (see below)

Slices cut from the deformed crystals were originally mounted on thin sections with an adhesive similar to *Crystal Bond* that softens quickly when heated. These mounts were not suitable for the polishing required for EBSD mapping. The adhesive surrounding the crystals was removed with acetone, leaving them fixed to the thin section in their original position. After applying a thin veneer of vacuum grease to the slide up to the edge of the crystal epoxy was poured in a 1" mount pressed against the glass slide with the crystal at the center. After hardening, the slide was removed on a hotplate.

The undeformed San Carlos olivine single crystal was set in an arbitrary orientation in epoxy and polished to 2500 grid on wet sandpaper. Polishing continued for both sample types on a vibratory polisher with an 0.05 µm alumina slurry for at least 6 h (sample thickness permitting), and finished with colloidal silica for about 1 h. The mounts were inserted in the SEM such that the compression direction was parallel to the *y*-axis of the map for 7506-2 (Fig. 2) and the long edges of the crystal parallel to the *x*-axis for 7406-2.

EBSD data acquisition and processing

Data acquisition

Diffraction (Kikuchi) patterns generated by elastic scattering of incoming electrons are captured by a CCD camera and processed for detection of bands (maxima in the Hough-transformed image). The set of angles between detected bands is compared to angles pre-calculated for the crystal structure of a set of preselected phases. The best match is recorded as the crystal orientation at that point. In the Oxford AZtec software, the residual error between detected and pre-calculated patterns is designated as mean angular deviation (MAD).

EBSD maps were acquired at the SUNY New Paltz Analytical Facility (semsunynp.com) with a TESCAN Vega 3 scanning electron microscope with LaB_6 filament, Nordlys Max 3 EBSD camera and Oxford Aztec V4.1 software. A 10 nm thick carbon coat was applied to all samples to avoid charging especially at small stepsizes. Additionally, carbon tape connected to the sample mount was placed near the mapped areas. Acquisition conditions and parameters were aimed at producing patterns with strong contrast, maximizing the number of detected bands and minimizing MAD. Therefore relatively high beam intensities were used such that the absorbed current on the tilted samples was 7–8 nA at 25 kV acceleration voltage and working distance of 18 mm. The CCD camera was positioned as close as practical to the sample, about 5 mm from the lower edge of the sample holder, to capture a large solid angle. No binning of patterns was applied as binning increases the angular uncertainty (Jiang et al. 2013). Acquisition frequencies with 60 bands in the match unit were between 20 and 33 Hz.

Two EBSD maps were acquired for 7506-2 from a slice of the deformed crystal cut parallel to the compression direction and perpendicular to [001]. Map 1 has a stepsize of 1 µm and 1197 × 1197 points, Map 2 a stepsize of 0.19 µm and 1570 × 1570 points. Mean MAD (0.25–0.26°), and average number of detected bands (9.8) were essentially the same for both maps. The top of Map 1 starts just below the top of the deformed crystal.

The slice from 7406-2 was cut perpendicular to the compression direction from the top of the crystal in contact with the tungsten deformation platen face. The slice was very thin and could not be polished to remove all scratches. A relatively coarse map of this sample has a stepsize of 1.5 µm, mean MAD of 0.24° and average number of detected bands of 9.97. A second map has a stepsize of 0.2 µm, mean MAD 0.25° with 9.97 detected bands. However, at the fine stepsize residual surface damage from polishing contributes significant noise. The results from this sample are summarized below and detailed in the Supplement.

Additionally, four maps of the as received (naturally deformed) San Carlos olivine single crystal were acquired with stepsizes of 0.2, 0.5, 1, and 2 µm.

Processing

The EBSD maps were processed with the MTEX Toolbox V5.6 (mtex-toolbox.github.io). Prior to calculation of dislocation densities noise needs to be smoothed. The aim for smoothing or 'denoising' of the data is to preserve real changes in orientation, but smooth noise related to band detection uncertainties and other noise (e.g., imperfections on the sample surface). Different filters for this purpose are discussed in Hielscher et al. (2019). Limited testing of different filters indicates that the most suitable filter is the 'total variation' functional with half-quadratic minimization (hQ filter). It preserves sharp sub-boundaries but smoothens isolated noise. Local filters such as the median or Kuwahara filter result in smoothed sub-boundaries and blocky appearance. Adjustable parameters for the hQ filter are a regularization parameter (α) and a threshold angle such that misorientation angles larger than this angle are not subject to denoising (kept at 5°).

The kernel average misorientation (KAM) is a measure of grain internal misorientation [e.g., Wright et al. (2011)]. KAM is calculated for each pixel from the sum of misorientations of a set number of neighboring pixels, normalized by the number of neighbors considered. The color scale for KAM maps can be set for saturation at a particular misorientation such that localized sub-boundaries appear as sharp lines. KAM maps, therefore, show similar structures as dislocation density maps, but based on the EBSD data without consideration of dislocation systems.

The computation of geometrically necessary dislocations from EBSD maps depends on local orientation changes in the map as discussed in Section "Dislocation geometry". The orientation changes are expressed by the curvature tensor, defined for every pixel in the EBSD map by the directional derivatives in x and y. As six components of the lattice curvature can be measured from 2-D EBSD maps, consideration of no more than six types of dislocations (four edge and two screw dislocations) results in a single, best fit solution for the densities of each type [see Wallis et al. (2016, 2017a) for further details and discussion]. The six types of dislocations were defined in MTEX for inversion of the curvature tensor to calculate the density of geometrically necessary dislocations following Pantleon (2008). In the rest of the manuscript, dislocation density refers to the calculated density of geometrically necessary dislocations, not the absolute dislocation density.

The relationship between dislocation density and angular change in orientation was examined along line traces in the maps. This allows more detailed investigation of the

contribution of the six dislocation types to angular change (residual strain). A calculated correlation coefficient between dislocation density and pixel to pixel angular change in orientation along the lines (shown in Table 2 and Figs. 11 and S5) is a measure of the linear dependence of the two variables, but the absolute value is influenced by smoothing. The correlation coefficients are intended to show the relative contribution of the different dislocation types to angular orientation change in concert with the relevant figures. The line directions are parallel to the two Burgers vectors considered here, since this is the direction of expected maximum curvature (Fig. 1). The line location was chosen to either avoid or explicitly include sub-boundaries.

Results

Denoising parameters and dislocation energy

The influence of different energy assignments for the dislocation types on calculated dislocation densities and structures is presented in the Supplement (Section 1). As detailed there, the assigned dislocation energy has little effect on calculated density, and no observable effect on structures. The smoothing parameter α does affect both calculated densities and observable structures (Supplementary Material Section 2). Too small values do not sufficiently smooth noise, artificially increasing dislocation densities and obscuring some structures. Too large values introduce artifacts and smooth real structures. With the above version of MTEX the hQ filter with a smoothing parameter of $\alpha = 5$ resulted in near minimal calculated dislocation densities for a given map, without introducing artificial structures [see also Hielscher et al. (2019)]. The value of the threshold angle does not affect calculated densities; coherent, sharp structures such as sub-boundaries with angular misorientation to 0.05° are preserved (Supplementary Material Section 3). Spatially distributed, gradual orientation changes with angular misorientation > 0.01° are above noise.

Noise floor

Wallis et al. (2016) mapped an undeformed San Carlos olivine single crystal to investigate the 'noise floor' of the technique. Similarly, an experimentally undeformed San Carlos olivine single crystal was mapped here at different stepsizes to establish a noise floor. Figure 3 shows that the apparent dislocation density increases as a function of decreasing stepsize for the undeformed crystal, similar to the observations of Wallis et al. (2016). At a stepsize of 1 µm, the dislocation density of deformed single crystal 7506-2 is significantly higher, while at a stepsize of 0.2 µm the dislocation densities are comparable.

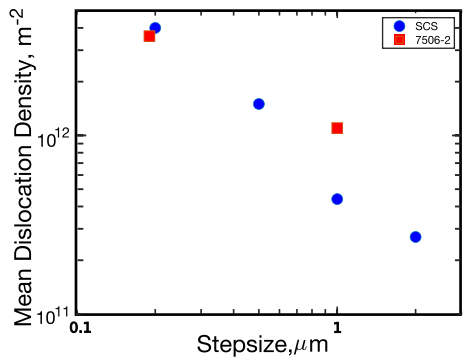

Fig. 3 Dislocation density as a function of stepsize for an experimentally undeformed San Carlos olivine single crystal and deformed sample 7506-2

Misorientation axes

Figure 4a shows the change in orientation of the crystal axes relative to the sample reference frame along Line 1 in Fig. 7b (below). [100] and [010] axes describe segments of great circles indicating rotation around [001]. This line traverses an area of the crystal with gradual angular orientation change without sub-boundaries. The angular change between neighboring pixels ranges between 0.01 and 0.03° (see Fig. 9a). Figure 4b shows the individual misorientation axes between neighboring points along this line. While individual axes can not be used to make inferences, the data overall clearly indicate [001] as the misorientation axis for the orientation change along this line, consistent with the rotation seen in Fig. 4a.

Prior (1999) examined the uncertainties of determining misorientation axes from conventional EBSD data. He showed that the uncertainty of individual misorientation axes increases substantially for misorientations < 5° such that they can not reliably be determined. However, he emphasized that the uncertainty decreases with increasing number of data. His dataset consisted of 30 misorientations, while the number of data here is nearly two orders of magnitude larger (for example, there are 1980 misorientation axes plotted in Fig. 4b).

Naturally deformed San Carlos olivine

The map acquired for the as received San Carlos single crystal with a 2 µm stepsize is shown in Fig. 5a. The coloring highlights sub-boundaries, with traces in the map that predominantly trend approximately perpendicular to the crystal [100] axis. Figure 5b shows that the misorientation angle relative to the first point of Line 1 (parallel to [100]) increases by ~ 1.5° across the prominent sub-boundaries up to the middle of the line, followed by a step-wise decrease of similar magnitude. Noticeable is the regular spacing of

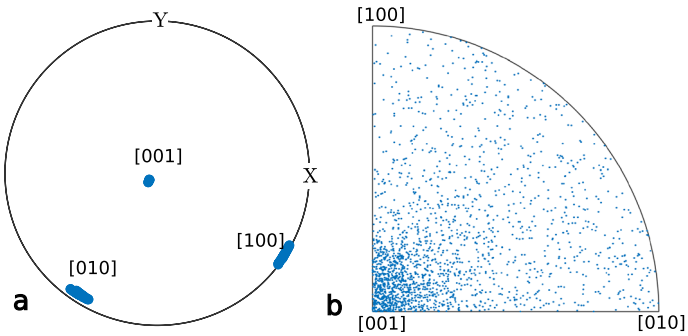

Fig. 4 **a** Pole figure showing orientation of crystal axes in sample coordinates for Line 1 in Fig. 7. **b** Misorientation axes in crystal coordinates between neighboring points of Line 1. Figure 9b shows the same distribution smoothed

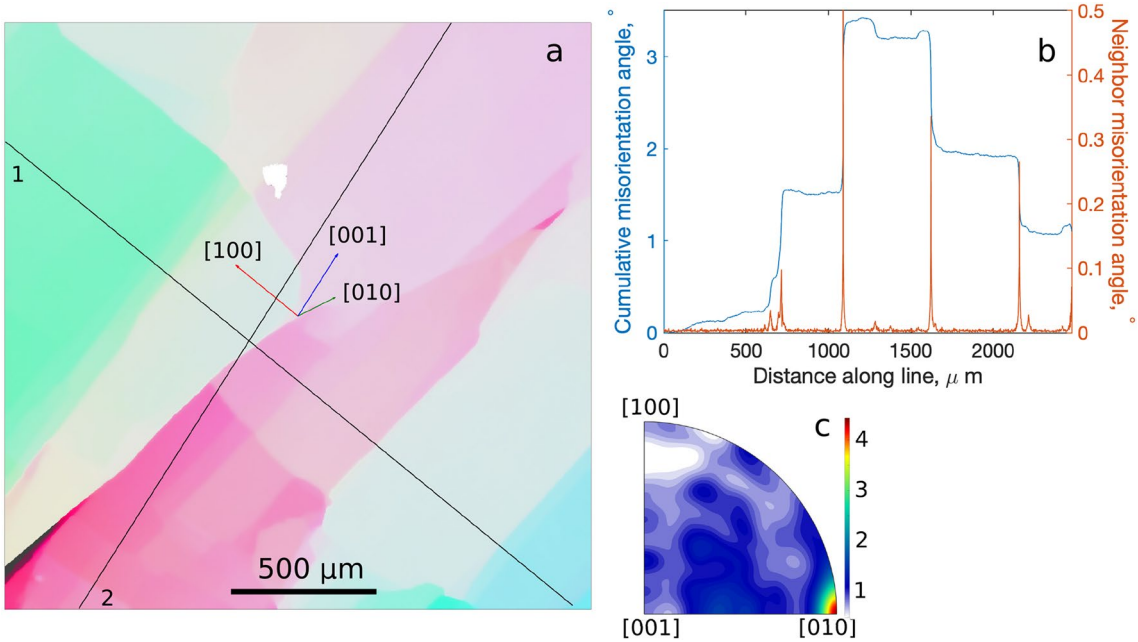

Fig. 5 **a** Map of SCS1 with color coding scaled to maximum misorientation. Crystallographic axes [100], [010] and [001] are shown by red, green and blue arrows, respectively. Black Line 1 indicates a transect parallel to [100] shown in (**b**). **b** Angular change in orientation along Line 1 in (**a**) relative to the first point of the line (left axis), and corresponding change in orientation between neighboring pixels (right axis). **c** Misorientation axes for neighbor orientation changes of Line 1

about 300 µm of the sub-boundaries [c.f. Durham et al. (1977)]. The right axis in Fig. 5b shows the angular change in orientation between neighboring pixels along the line. The corresponding misorientation axes are clustered near [010] (Fig. 5c).

The dislocation density maps calculated from the data in Fig. 5a are shown in Fig. 6. [100](001) edge dislocations most prominently form sub-structures, while screw dislocations are only observed in the sub-boundaries with largest angular change. Sub-boundaries perpendicular to crystallographic [100] consist predominantly of edge dislocations with **b** = [100] Burgers vector. Correspondingly, angular orientation changes along Line 1 are best correlated with this Burgers vector (Table 2). Sub-boundaries (near) perpendicular to [001] are dominantly formed by **b** = [001] dislocations, with no contribution from [100](010). No single dislocation type is particularly well correlated with angular change for the crystallographic [001] direction (Line 2). Misorientation axes for both lines cluster around [010] (Fig. 5c), consistent with the dominance of [100](001) edge dislocations. Screw dislocations are notably uncorrelated with orientation changes (Table 2), indicating that the sub-boundaries are tilt boundaries.

Deformed [110]c sample 7506-2

Figure 7 shows the microstructure of [110]c sample 7506-2. The color scheme in Fig. 7a is calculated from the misorientation axis at each point to the mean orientation of the crystal. The dominantly red colors indicate rotation

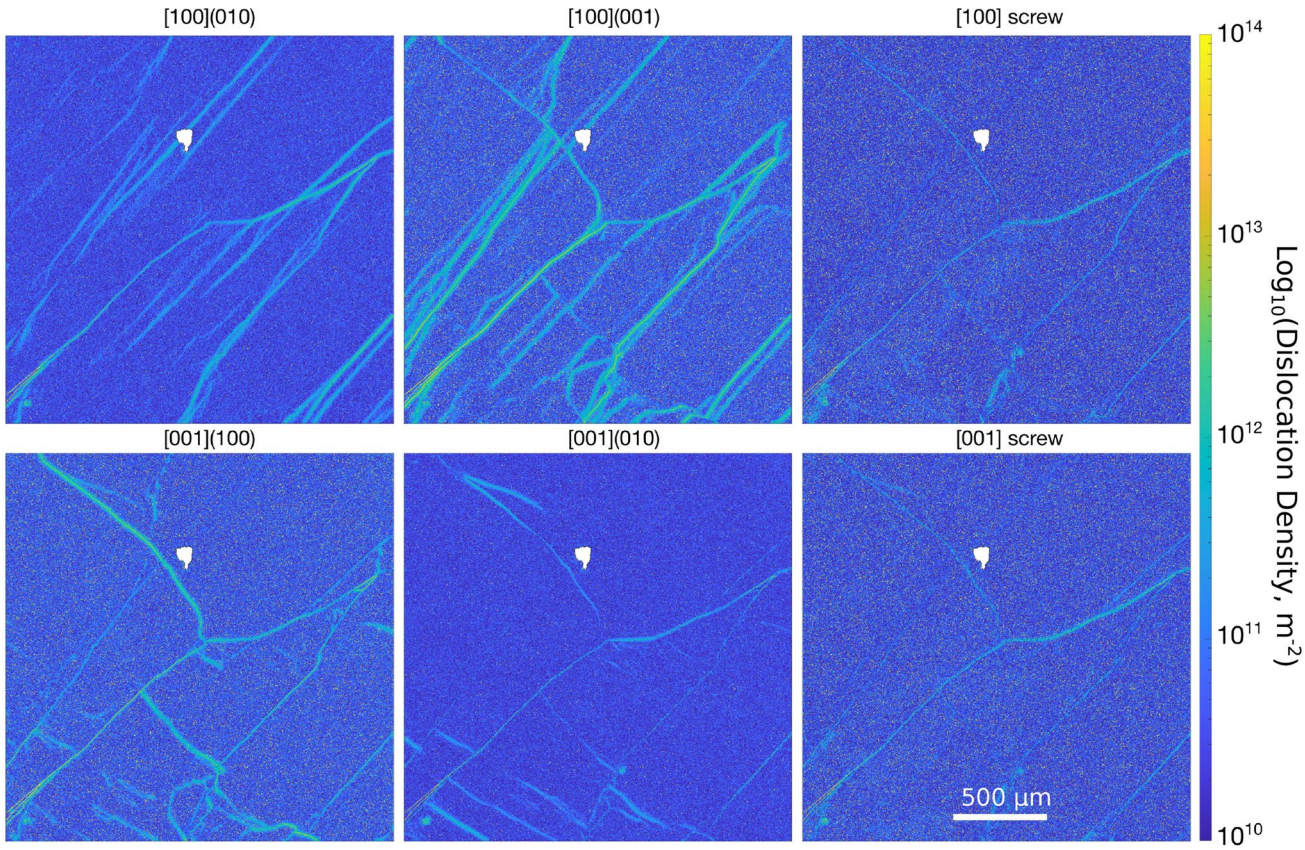

Fig. 6 Dislocation densities of the six dislocation types for SCS1 at a stepsize of 2 µm. A not-indexed area appears white. In addition to subboundaries on traces of planes near (100) there are also (mostly shorter) sub-boundaries near traces of (001) planes. The maps for [100](010) and [001](010) edge dislocations are significantly less noisy for this orientation of the single crystal than the maps of the other dislocation types

Table 2 Correlation between change in orientation and dislocation density along lines

Sample	Figure (Line)	step (µm)	c. dir.	max (°)	[100] (010)	[100] (001)	[001] (100)	[001] (010)	[100] screw	[001] screw
SCS1	5(1)	2	[100]	3.4	0.53	0.67	0.40	0.29	0.21	0.26
SCS1	5(2)		[001]	2.9	0.20	0.39	0.33	0.28	0.19	0.17
7506	7(1), 9	1	[100]	6.0	0.82	0.29	0.45	0.11	0.38	0.41
7506	7(2), 12		[010]	1.8	0.24	0.61	0.55	0.42	0.69	0.62
7506	7(3)			5.4	0.26	0.0	0.21	0.05	0.33	0.32
7506	13(1)	0.19	[100]	13.8	0.59	0.46	0.29	0.29	0.59	0.57
7506	13(2)		[100]	5.0	0.57	0.04	0.19	0.08	0.15	0.13
7406	S 2(2), S 4	1.5	[100]	3.1	0.56	0.23	0.14	0.42	0.50	0.41
7406	S 2(1)		[001]	1.7	0.40	0.44	0.56	0.67	0.64	0.62

c. dir. indicates the crystallographic direction of the lines.

max ° shows the maximum angular change relative to the first point of a line

around [001] (c.f. Fig. 4). The sharp change from red to yellow colors is due to a near horizontal sub-boundary with misorientation axis between [001] and [010]. A second, less prominent sub-boundary running near horizontally near the center of the map is faceted or stair-stepped. The angular orientation change of the deformed crystal is illustrated in Fig. 7c.

Figure 7b shows kernel average misorientation calculated for the same area. The KAM map indicates magnitude and location of local orientation changes. Yellow colors indicate

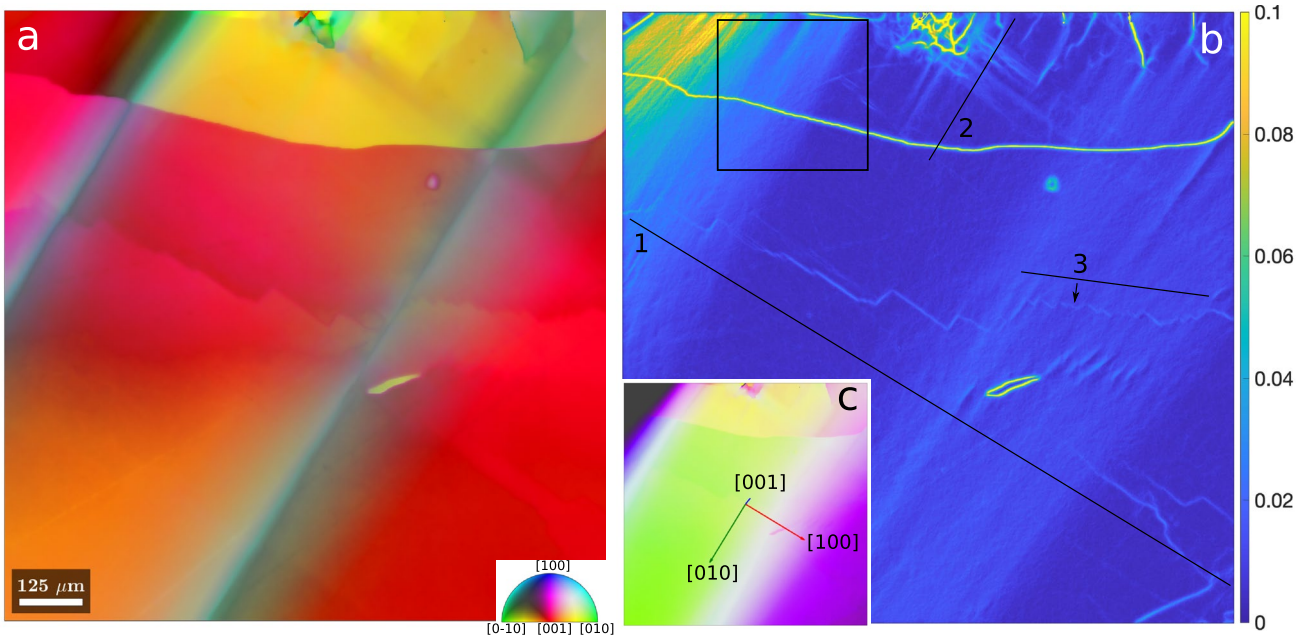

Fig. 7 **a** EBSD map of the plane strain section of deformed single crystal 7506-2 of Durham and Goetze (1977) with a stepsize of 1 µm covering a 1.2 × 1.2 mm area. Color coding displays rotation from the mean orientation around [001] by red, around [010] by green and [100] by blue colors (inset). Compression direction was vertical in the plane of the page. The top of the map is close to the top of the deformed crystal, with incipient recrystallization. **b** Kernel average misorientation (KAM) map. Colorscale represents angular misorientation capped at 0.1°. The bulk of the crystal shows relatively broad and diffuse bands of high KAM approximately parallel to the crystal [010] direction. Black lines indicate transects further discussed below. Line 3 is shown offset from the faceted sub-boundary. Black square indicates the map shown in Fig. 13. **c** Map with color coding emphasizing the angular orientation change, most prominently in the direction of the crystal [100] axis. Crystallographic axes representing the mean orientation of the crystal are shown by arrows

the largest misorientations to neighboring pixels, light blue colors comparatively smaller misorientations. Near diagonal, diffuse bands roughly parallel to [010] are prominent, corresponding to changes in orientation parallel to the [100] direction across the crystal (Fig. 7c). Sharp, horizontal lines correspond to the sub-boundaries in Fig. 7a. High KAM values are also observable at the top of the map. The KAM map represents the underlying data for the calculated dislocation densities discussed next.

Dislocation density maps

Figure 8 shows dislocation densities for each of the six dislocation types considered. All show some activity, but the smooth orientation change and sub-boundaries observable in the orientation maps (Fig. 7) are formed by different dislocation types.

Most prominent in the mapped area are broad bands oriented parallel to the crystal [010] axis of high dislocation density of [100](010) edge dislocations. This glide system was designed to have the highest Schmid factor by the deformation geometry (Table 1). The bands correspond to the diffuse bands of higher KAM (Fig. 7b) and the gradual change in angular orientation of the crystal best seen in Fig. 7c. It should be noted that individual [100](010) dislocations arranged in slip bands parallel to [100], schematically shown in Fig. 1 and imaged in oxidatively decorated sections (e.g., Durham et al. (1977) their Fig. 1a), are not imaged here. Rather, the map shows the variability in the density of these dislocations parallel to the crystal [100] axis that results in the macroscopic orientation change of the crystal lattice detailed below.

The next most prominent pattern are inverted V-shaped 'rays' originating from the top of the sample in directions roughly parallel to the crystal [010] and [100] axes. These rays are well defined for both screw dislocations, but only the right arm (parallel to the [100] axis) is partially expressed for some edge dislocations. Shorter, finger-like high dislocation densities also originating from the top are more or less strongly expressed for all dislocation types. Both patterns may originate with inhomogeneous stresses at the deformation platen–sample interface (e.g., friction during the experiment or on cooling).

Two sub-boundaries extending near horizontally across the map are most prominently expressed in the densities of screw dislocations, with contributions from [100](001) and [001](100) edge dislocations. [100](010) edge

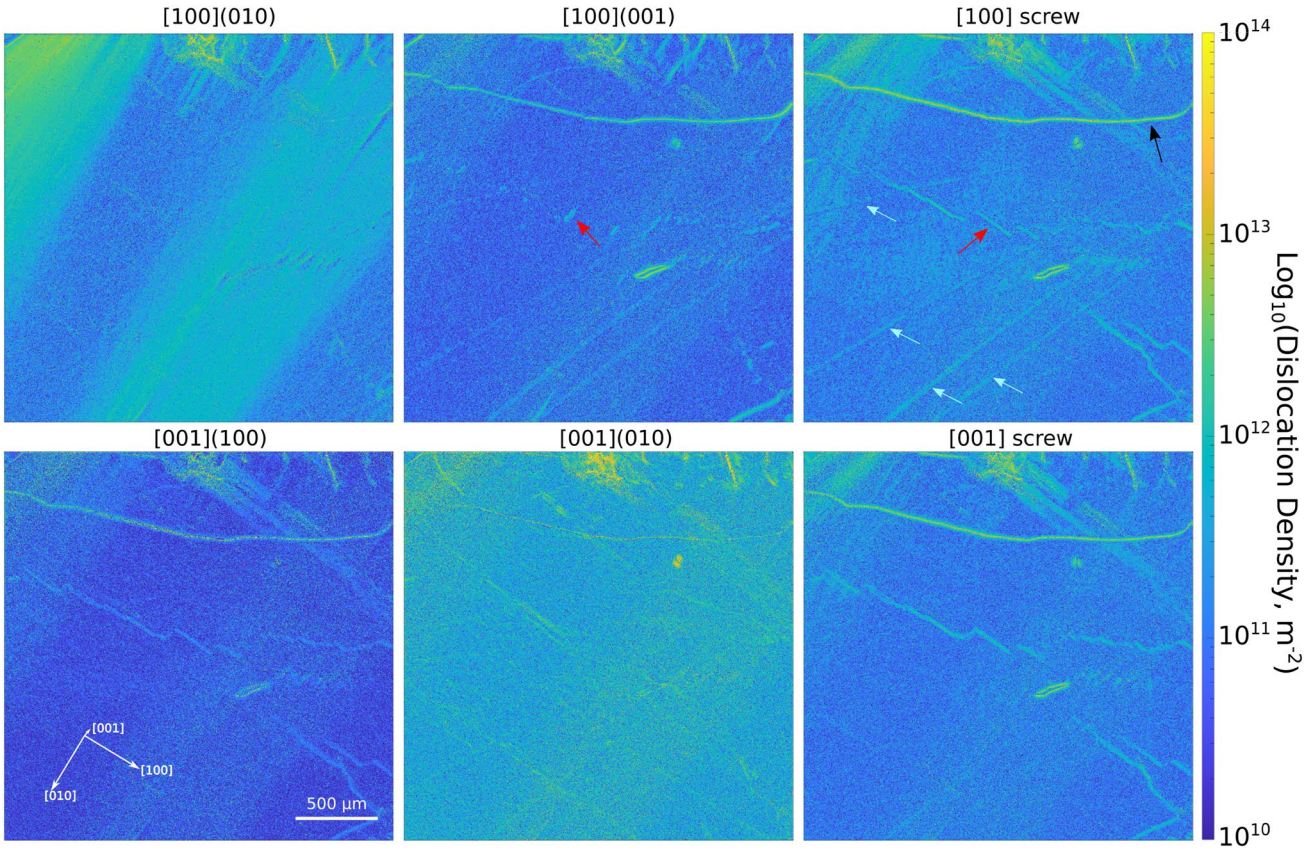

Fig. 8 Dislocation densities of the six dislocation types of 7506-2. The black arrow indicates a continuous sub-boundary with a misorientation > 1° across it. Red arrows indicate a stair-stepped or faceted sub-boundary also visible in Fig. 7a. Light blue arrows indicate polishing imperfections (scratches) observable mainly by the [100](001) slip system

dislocations do not contribute significantly to the formation of the sub-boundaries.

Dislocation structures and misorientation

The relationship between dislocation density and change in orientation of the crystal, reflecting accumulated angular strain, can be examined along lines extracted from the maps. Figure 9a shows angular change in orientation and orientation gradient (neighbor to neighbor misorientation angle) along Line 1 parallel to [100] in Fig. 7b. The bands of high dislocation density first cause an increase in misorientation angle, followed by a decrease so that the net change in orientation of the crystal along the line is modest. The corresponding neighbor to neighbor misorientation axes in Fig. 9b are strongly clustered near the [001] crystallographic axis (c.f. Fig. 4), consistent with [100] (010) edge dislocations.

Dislocation density related to the change in orientation of the crystal along Line 1 is further examined in Fig. 10. This figure shows correlation of dislocation density of individual dislocation types with change in orientation. The correlation coefficients shown in Fig. 10 and Table 2 are calculated after smoothing of both dislocation density and change in orientation along the line. Consistent with the misorientation axes in Fig. 9b, [100](010) is best correlated with the change in orientation. [001](010) has the highest average dislocation density but is poorly correlated with the change in orientation. Modest correlation of the other dislocation types is due to more localized changes in orientation near the end of the Line.

Another view of the relationship between dislocation density and angular change in orientation of Line 1 is shown in Fig. 11. Comparison with Fig. 9a shows that the change in angular orientation between 1–200 and 600–1200 µm is due to high density of spatially distributed [100](010) edge dislocations. [001](010) edge dislocations are uncorrelated with angular change in orientation.

The structure of the more localized concentrations of dislocations near the top of the crystal, including sub-boundaries, is examined by Line 2 in Fig. 7b. The sharp change in orientation in Fig. 12a across the sub-boundary is due to [100](001) and [001](100) edge dislocations along with both types of screw dislocations (Fig. 8, Supplementary

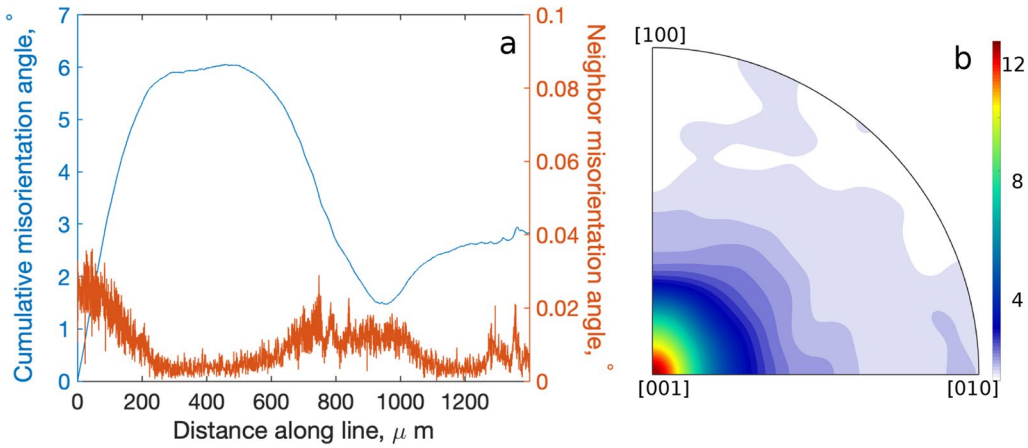

Fig. 9 **a** Angular change in orientation along Line 1 in Fig. 7b relative to the first point of the line (left axis), and corresponding change in orientation between neighboring pixels (right axis). This line does not cross a sharp sub-boundary. **b** Smoothed distribution of misorientation axes in crystal coordinates for the change in orientation between neighboring points in (**a**). The same data are plotted as individual misorientation axes in Fig. 4

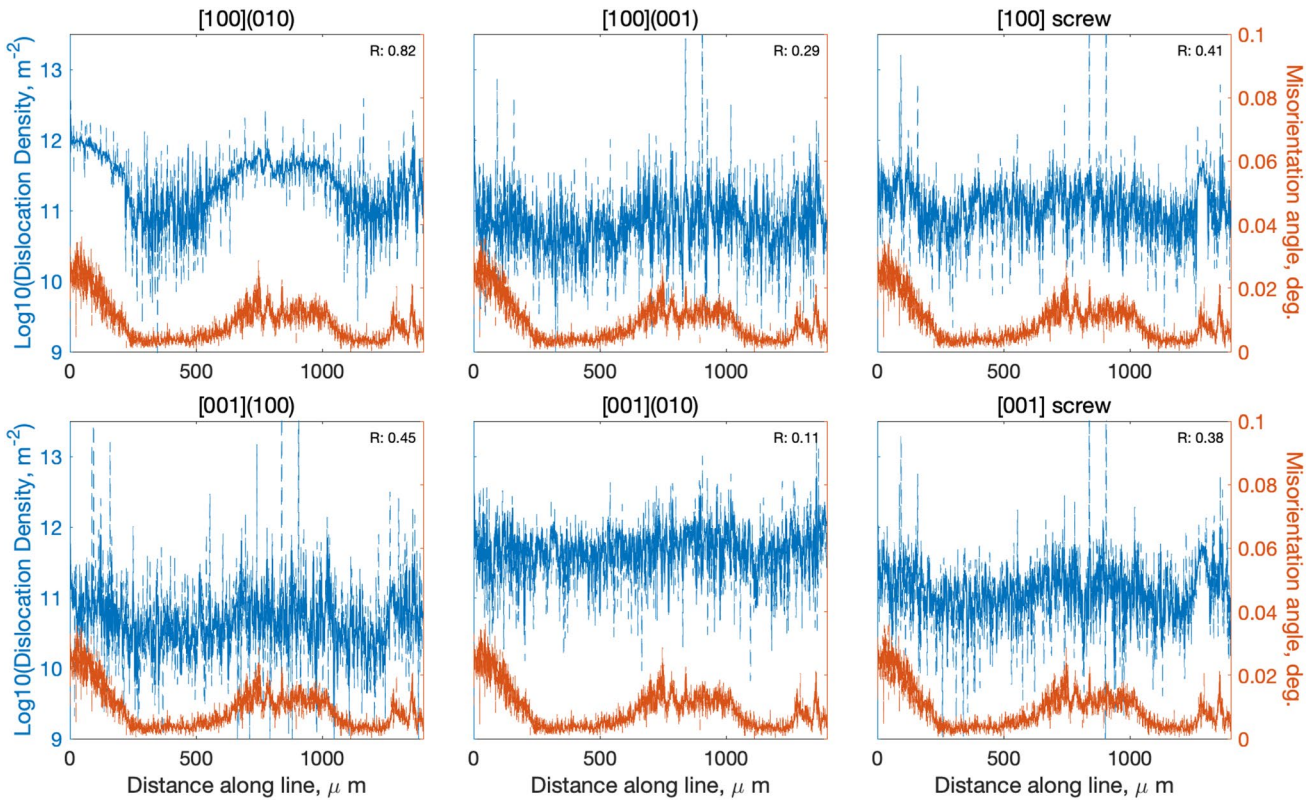

Fig. 10 Correlation of dislocation density for the six dislocation types with angular change between neighbor pixels along Line 1. The correlation coefficient shown in the top right of each panel is calculated after smoothing (solid line) of the raw data (dashed). [100](010) is best correlated with the angular change, following the broad gradients. [001](010) has the highest average dislocation density but does not correlate with angular change. Correlation of the other dislocation types also includes more localized changes in angular orientation towards the end of the line

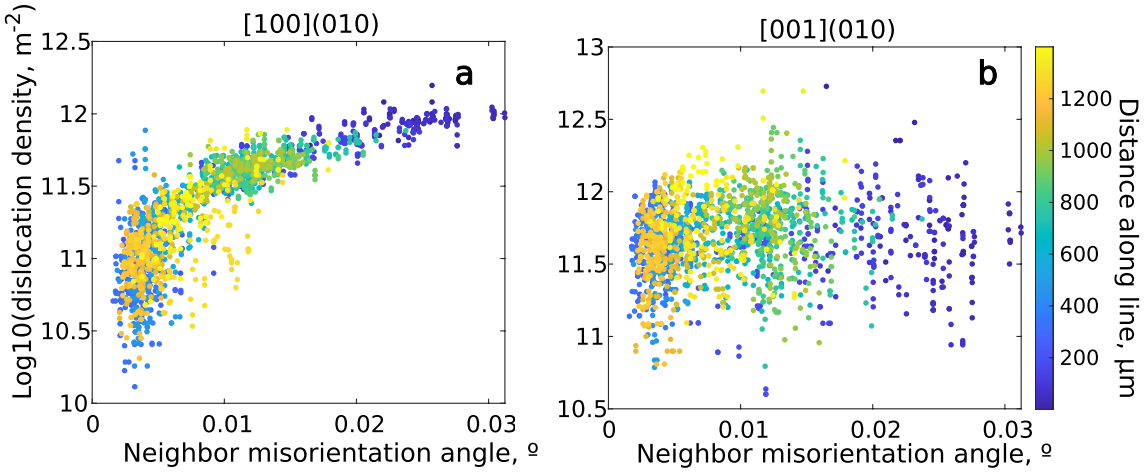

Fig. 11 Dislocation density plotted against angular change in orientation between neighboring pixels, color coded by distance from the first point of Line 1, Fig. 7b (in µm). **a** [100](010) is well correlated with angular orientation change, **b** [001](010) is uncorrelated

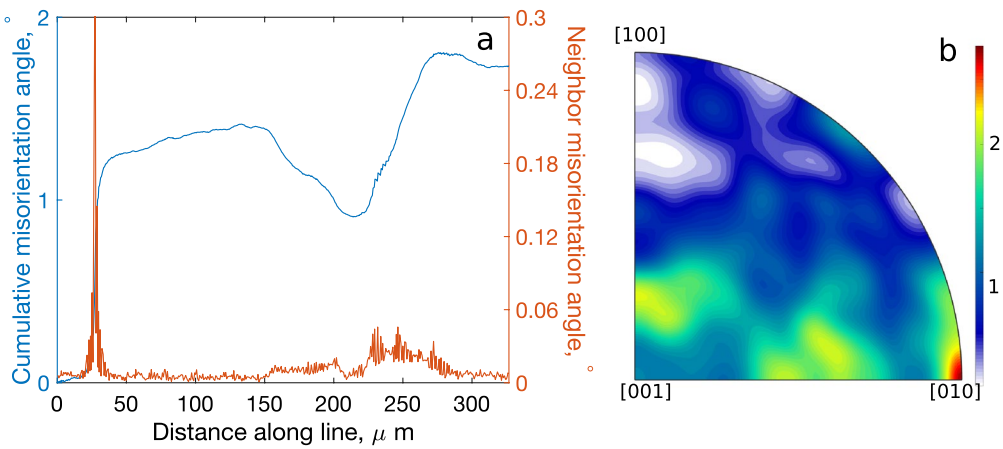

Fig. 12 **a** Angular change in orientation along Line 2 in Fig. 7b relative to the first point of the line (left axis), and corresponding gradient between neighboring pixels (right axis). The localized change in orientation at the beginning of the line is due to a sub-boundary. **b** Misorientation axes in crystal coordinates for the change in orientation between neighboring pixels. The axes for Line 2 are spread between [001] and [010]

Figure 2). Misorientation axes are clustered at [010] in Figure 12b, consistent with the two minor slip systems (but compare maximum MUD value to that in Fig. 9b). Along the rest of the line screw dislocations dominate the inverted V-shaped rays of high dislocation densities. Screw dislocations are best correlated with orientation changes along the line (Table 2). They account for the spread of misorientation axes between [001] and [010] in Fig. 12b.

Line 3 follows the faceted sub-boundary with segments parallel to [100] and [010]. Angular orientation change is best correlated with dislocation density of the screw dislocations, with little involvement of edge dislocations (Table 2).

The second map with high spatial resolution, near the top left corner of the larger map in Fig. 7 is shown in Fig. 13. The angular change in orientation along Line 1 in this figure is more than twice that of Line 2. For Line 1, which includes the sub-boundary, screw dislocations along with [100](010) edge dislocations are best correlated with the change in angular orientation. For Line 2 without a sub-boundary only [100](010) is correlated with angular change (Table 2).

Close inspection of the near horizontal sub-boundary in this map shows that it is faceted at a small scale (Supplementary Fig. 3). Similar to the more obviously faceted sub-boundary in Fig. 8 facets parallel to the crystal [010] direction consist predominantly of [100](001) edge dislocations, while facets near the crystal [100] direction consist predominantly of both types of screw dislocations, with

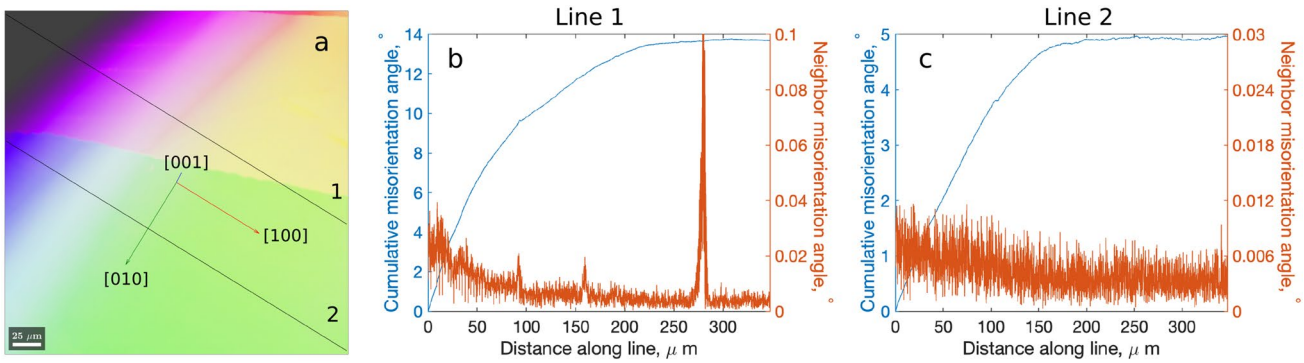

Fig. 13 **a** Map with high spatial resolution (0.19 μm stepsize) of 7506-2 indicated by the square in Fig. 7. **b**, **c** Angular change in orientation relative to the first point of the line (left axis), and neighbor pixels angular change in orientation (right axis) along the two lines in (**a**). Line 1 includes the prominent sub-boundary, as well as a number of smaller 'spikes' in orientation change. Note the difference in the scale of orientation change (right axis) in this and other figures

contributions from both **b** = [001] edge dislocations. [100](010) dislocations are absent for this sub-boundary.

Deformed [011]c sample 7406-2

The slice mapped from this sample is a transverse section from the top of the deformed crystal, adjacent to the platen (Supplementary Fig. 4). Orientation changes and dislocation patterns in maps from this section are less distinctive and affected by friction between crystal and platen. Dislocation densities are further affected by scratches that could not be removed by polishing due to the thinness of the slice. Calculated dislocation densities show that the intended slip system for this orientation [001](010) has the most coherent structures and highest density of dislocations (Suplementary Figure 5). Misorientation axes in a line traverse parallel to [001] are clustered near [100], consistent with this slip system (Suplementary Figure 6). Orientation changes along this line are best correlated with [001](010), and uncorrelated with **b** = [100] edge dislocations (Supplementary Fig. 7, Table 2).

Discussion

Uncertainties and noise

Jiang et al. (2013) examined the noise floor (or minimum measurable value) for HR-EBSD measurements of dislocation density. They relate the lower bound to angular resolution divided by stepsize times length of Burgers vector. If the mean MAD value for the maps is substituted for angular resolution, the calculated noise floor at a stepsize of 1 μm is $\sim 8 \times 10^{11}$ m^{-2}. With the denoising described above, the noise floor determined for the naturally deformed San Carlos single crystal is about half of this value (Fig. 3).

Wallis et al. (2019b) show a noise level in the point to point misorientation angles of a line traverse across an undeformed olivine sample with conventional EBSD of about 0.1° (their Fig. 4). The noise level in this study is about one order of magnitude lower, comparable to that shown for HR-EBSD, both at relatively large stepsize (1 μm, e.g., Figs. 9, 10, and 12), but also at 0.19 μm stepsize (Fig. 13).

Calculated values of dislocation density are influenced by denoising methods and their parameters applied prior to calculation of dislocation density (see Supplement). No filtering was applied by Wallis et al. (2016, 2017a). They also discuss limitations regarding the absolute value of dislocation densities obtained from EBSD mapping in comparison to oxidative decoration. With these caveats (as well as a higher final flow stress of Wallis et al. (2017a)) average total dislocation densities calculated here are of the same order of magnitude, about 10^{12} m^{-2} at 1 μm stepsize.

Noise for individual dislocation types depends on the orientation of the plane of the section relative to the crystallographic axes (Wallis et al. (2019a)). For [110]c sample 7506-2 **b** = [001] edge dislocations are near perpendicular to the plane of the plane strain section. These edge dislocations do not cause changes in orientation in this plane and are therefore not detectable (Fig. 1). Wallis et al. (2016, 2019a) point out that noise in this case can cause spurious high dislocation density. The (uniformly) high dislocation density for [001](010) edge dislocations seen in Fig. 8 is, therefore, likely an artifact and is not included in the average dislocation densities discussed above. Similarly, the full curvature of screw dislocations with Burgers vectors in the plane of observation is not detectable.

Comparison with observations of Durham and Goetze (1977) and Durham et al. (1977)

An aim of the single crystal deformation experiments is to generate uniform strain across the crystal (Durham and

Goetze 1977). For uniform strain, changes in orientation ideally are accommodated by a homogeneous distribution of dislocations of the slip system with the highest Schmid factor. Durham et al. (1977) show that a steady-state dislocation density (of mobile dislocations) is reached after a few % strain. On further deformation canting of the crystals (change of the shape from rectangular prism to parallelepiped) is frequently observed at strains above about 10% for [110]c and [011]c orientations (Durham and Goetze (1977), their Table 4).This indicates that strain and hence stress and consequently dislocation density is no longer uniform across the crystal. This is confirmed here by the observation of 200–300 µm wide bands of alternating high and low dislocation density of [100](010) edge dislocations in the [110]c sample (Fig. 8). By comparison the typical image width showing decorated dislocations is < 150 µm [e.g. Durham et al. (1977), Bai and Kohlstedt (1992), Wallis et al. (2017a)].

For a line perpendicular to these bands the misorientation angle increases across the first band, then decreases across the second band (Fig. 9). This implies that the dislocations within each of the bands are of like polarity, and that the two bands contain dislocations of opposite polarity. Durham and Goetze (1977) pointed out that lattice distortion due to canting is effected by spatial segregation of edge dislocations of the active slip system. They characterized the lattice distortion by an 'axis of external rotation', which is coincident with the line direction of the edge dislocations involved (in this case [001]), consistent with the misorientations axes in Fig. 9b (see also Fig. 4a).

Depending on location and endpoints of lines across the crystal misorientation angles up to 14° are determined from the EBSD maps (Table 2). This compares with an angle of lattice rotation, $\alpha = 9° \pm 9°$, observed by Durham and Goetze (1977) (their Table 4).

Since screw dislocations are not restricted to a particular glide plane, $\mathbf{b} = [100]$ screw dislocations can have misorientation axes in the range between [010] and [001] (c.f. Fig. 12b). Misorientation axes in this range are usually attributed to 'pencil glide' on [100](0*kl*) planes (Raleigh 1968). However, Durham et al. (1977) did not observe discrete glide planes between (010) and (001) and noted that cross slip of [100] screw dislocations could give the appearance of pencil glide (Poirier 1975). Mahendran et al. (2019) concluded from ab initio modeling that the cores of [100] screw dislocations can spread on {021} planes, giving the appearance of pencil glide.

The bands of high density of [100](010) edge dislocations in Fig. 8 discussed above continue across the prominent sub-boundary formed by screw and [100](001) and [001](100) edge dislocations. This suggests limited interaction between the dislocation systems (Durham et al. 1985).

Comparison with other studies

Demouchy et al. (2013) describe 'strongly misoriented zones' in single crystals deformed at 300 MPa confining pressures but significantly lower temperatures (predominantly 800–900 °C). Their EBSD maps and line traverses show that in these zones the lattice orientation rotates progressively by similar magnitudes and distances as described here (Fig. 9). TEM observations show a progressive increase in dislocation density in the zones but no sub-boundaries or kink bands. Similar to 7506-2 (Fig. 8) predominantly dislocations of one slip system are observed in the strongly misoriented zones. At lithospheric temperatures (below approximately 1000 °C) slip systems with $\mathbf{b} = [001]$ dominate deformation (Demouchy et al. 2013; Mussi et al. 2015).

HR-EBSD maps of Wallis et al. (2017a) show similar gradients in orientation parallel to the direction of the intended dominant Burgers vector in the off-diagonal components of the antisymmetric rotation tensor ω_{12} for samples deformed in [110]c and ω_{23} for [011]c, respectively. Their maps of dislocation densities, however, show narrow bands of alternating high and low dislocation density, predominantly for glide systems with low Schmid factor. Wallis et al. (2017a) attribute the lack of observable [100](010) dislocations in the [110]c experiment deformed at 1200 °C to a misalignment of the crystal axes from the intended orientation. Similarly, the crystals discussed here are not perfectly aligned relative to the intended orientations.

Comparatively narrow, ray shaped, alternating bands of high and low dislocation density can be seen near the top of the [110]c crystal in Fig. 8. These bands are sampled by Line 2 in Fig. 7. They possibly resemble the sets of parallel bands observed by Wallis et al. (2017a), and similarly consist predominantly of screw dislocations as well as [100](001) and [001](100) edge dislocations. Wallis et al. (2017a) discuss narrow bands of dislocations of opposite sign and therefore no net change in orientation as 'dipolar mats'. The bands observed here, however, consist of dislocations of the same sign, increasing the misorientation across them (Fig. 12a).

Sub-boundaries

For the as received San Carlos olivine Durham et al. (1977) noted a network of sub-boundaries in the three principal planes, similar to those observed here. Gueguen (1979) also described a cell structure with low density of free dislocation in the interiors of the cells. The cells are bounded by (100) and (001) tilt walls consisting of edge dislocations (Durham et al. 1977), as well as (010) twist walls consisting of screw dislocations (Durham et al. 1977; Darot and Gueguen 1981). The latter are not observed here.

Inspection of Fig. 7 shows that the less pronounced sub-boundary consists of facets with segments close to parallel

to the [100] and [010] crystal directions. For the prominent, apparently smooth sub-boundary at 1 µm stepsize (Fig. 8) faceting becomes apparent at 0.19 µm stepsize along at least some of its length (Supplementary Fig. 2). For both sub-boundaries the segments near parallel to the crystal [100] direction consist predominantly of screw dislocations, the segments near parallel to the crystal [010] direction consist of [100](001) edge dislocations. Dislocations of the main slip system of this deformation geometry are notably absent. Nets of [100] and [001] screw dislocations forming twist boundaries in the (010) plane were also observed in decorated sections and TEM (Durham et al. 1977; Darot and Gueguen 1981; Bai and Kohlstedt 1992).

Similar faceted sub-boundaries were observed by Bai and Kohlstedt (1992) both for [110]c and [011]c samples. They inferred that the faceted sub-boundaries predated experimental deformation and were in the process of decomposition during the experiments. However, Durham et al. (1977) noted that pre-existing sub-boundaries were rapidly destroyed and effectively erased after ~ 2% strain. The samples mapped here experienced 29% (7506-2) and 21 % (7406-2) strain. While the individual segments are parallel to crystallographic low index planes, their different lengths results in an overall orientation of the sub-boundaries that is more aligned with the plane of the deformation platens.

Gueguen and Darot (1982) showed from TEM observations that dislocations with [001] line direction in a deformed [110]c sample were not all **b** = [100] edge dislocations but some were **b** = [001] screw dislocations. They noted that misalignment of the crystal due to sub-boundaries can lead to activation of other slip systems. The high strain region near the top of the [110]c sample includes **b** = [001] Burgers vectors (Fig. 8).

Conclusions

The results presented here show that conventional EBSD mapping can be used to investigate dislocation structures in deformed olivine samples, provided they are well polished, and accuracy of indexing is prioritized during acquisition. Following denoising, these maps enable identification of dislocation types forming grain internal structures. Correlation of dislocation types with angular change in the deformed crystals relate this grain internal structure to macroscopic (angular) strain. This illustrates that distributed dislocations generate most of the macroscopically observed angular strain at least in the crystals examined, and that these dislocations are preserved during quench. Misorientation axes for orientation change above a few one-hundreds of one degree can be resolved in a statistical sense.

Due to less intensive computational requirements in comparison to HR-EBSD, larger areas can be mapped, providing a more representative view of deformation structures in coarse-grained aggregates. While decreasing step size increases the noise floor, the structure of sub-boundaries with high dislocation density can be resolved, which maybe missed at coarser stepsize.

In both the naturally and experimentally deformed crystals mapped the misorientation angle first increases and then almost completely reverses along lines parallel to the crystal [100] axis. While the orientation change in the deformed [110]c crystal is primarily due to broad bands of distributed [100](010) edge dislocations, in the naturally deformed crystal this change in orientation is due to sub-boundaries consisting of both types of **b** = [100] edge dislocations. The absence of detectable distributed dislocations in the natural samples suggests low stress levels prior to transport to the surface.

Supplementary Information The online version contains supplementary material available at https://doi.org/10.1007/s00269-021-01157-3.

Acknowledgements I thank William Durham for providing slices of deformed single crystals from his collection. I also thank William and Gordana Garapić for insightful discussions of dislocation structures and geometry. Sylvie Demouchy and an anonymous reviewer are thanked for their detailed and constructive reviews. I thank Martin Rutstein for his efforts to support the SUNY NP SEM lab. Support from NSF Grant EAR-2125895 is gratefully acknowledged.

Data availability Raw EBSD maps are available at 10.5281/zenodo.5130629

Declarations

Conflict of interest The author declares that he has no conflict of interest.

Open Access This article is licensed under a Creative Commons Attribution 4.0 International License, which permits use, sharing, adaptation, distribution and reproduction in any medium or format, as long as you give appropriate credit to the original author(s) and the source, provide a link to the Creative Commons licence, and indicate if changes were made. The images or other third party material in this article are included in the article's Creative Commons licence, unless indicated otherwise in a credit line to the material. If material is not included in the article's Creative Commons licence and your intended use is not permitted by statutory regulation or exceeds the permitted use, you will need to obtain permission directly from the copyright holder. To view a copy of this licence, visit http://creativecommons.org/licenses/by/4.0/.

References

Bai Q, Kohlstedt DL (1991) High-temperature creep of olivine single crystals 1. Mechanical results for buffered samples. J Geophys Res 96:2441–2463

Bai Q, Kohlstedt DL (1992) High-temperature creep of olivine single crystals 2. Dislocation structures. Tectonophysics 206:1–29

Britton TB, Wilkinson AJ (2012) High resolution electron backscatter diffraction measurements of elastic strain variations in the

presence of larger lattice rotations. Ultramicroscopy 114:82–95. https://doi.org/10.1016/j.ultramic.2012.01.004

Britton T, Birosca S, Preuss M, Wilkinson A (2010) Electron backscatter diffraction study of dislocation content of a macrozone in hot-rolled Ti-6Al-4V alloy. Scripta Mater 62:639–634

Cordier P, Demouchy S, Beausir B, Taupin V, Barou F, Fressengeas C (2014) Disclinations provide the missing mechanism for deforming olivine-rich rocks in the mantle. Nature 507:51–56

Darot M, Gueguen Y (1981) High temperature creep of forsterite single crystals. J Geophys Res 86:6219–6234

Demouchy S, Tommasi A, Boffa Balleran T, Cordier P (2013) Low strength of Earth's uppermost mantle inferred from tri-axial deformation experiments on dry olivine crystals. Phys Earth Planet Inter 220:37–49

Durham WB, Goetze C (1977) Plastic flow of oriented single crystals of olivine 1. Mechanical data. J Geophys Res 82:5737–5753

Durham WB, Goetze C, Blake B (1977) Plastic flow of oriented single crystals of olivine 2. Observations and interpretations of dislocation structures. J Geophys Res 82:5755–5770

Durham WB, Ricoult DL, Kohlstedt DL (1985) Interaction of slip systems in olivine. In: Schock RN (ed) Point defects in minerals, vol 31. American Geophysical Union, Washington, DC, pp 185–193

Farla RJM, Gerald JDF, Kokkonen H, Halfpenny A, Faul UH, Jackson I (2011) Slip-system and EBSD analysis on compressively deformed fine-grained polycrystalline olivine. In: Prior DJ, Rutter EH, Tatham DJ (eds) Deformation mechanisms, rheology and tectonics: microstructures, mechanics and anisotropy, vol 360. Geological Society, London, pp 225–235 (**Special Publications**)

Fujino K, Nakazaki H, Momoi H, Karato S, Kohlstedt D (1993) TEM observation of dissociated dislocations with **b** = [010] in naturally deformed olivine. Phys Earth Planet Inter 78:131–137

Gueguen Y (1979) Dislocations in naturally deformed terrestrial olivine: classification, interpretation, applications. Bull Minéral 102:178–183

Gueguen Y, Darot M (1982) Les dislocations dans la forstérite déformée à haute température. Philos Mag A 45:419–442. https://doi.org/10.1080/01418618208236180

Hielscher R, Silbermann CB, Schmidl E, Ihlemann J (2019) Denoising of crystal orientation maps. J Appl Crystallogr 52:984–996. https://doi.org/10.1107/S1600576719009075

Hirth G, Kohlstedt DL (2003) Rheology of the upper mantle and the mantle wedge: a view from the experimentalists. In: Eiler J (ed) Inside the subduction factory, Geophysical Monographs, vol 138. American Geophysical Union, Washington DC, pp 83–105

Jaoul O, Michaut M, Gueguen Y, Ricoult D (1979) Decorated dislocations in forsterite. Phys Chem Miner 5:15–19

Jiang J, Britton T, Wilkinson A (2013) Measurement of geometrically necessary dislocation density with high resolution electron backscatter diffraction: effects of detector binning and step size. Ultramicroscopy 125:1–9. https://doi.org/10.1016/j.ultramic.2012.11.003

Karato S, Lee KH (1999) Stress-strain distribution in deformed olivine aggregates: inference from microstructural observations and implications for texture development. In: Proceedings of the twelfth international conference on textures of materials, pp 1546–1555

Kohlstedt DL (1976) New technique for decorating dislocations in olivine. Science 191:1045

Kröner E (1958) Kontinuumstheorie der Versetzungen und Eigenspannungen. Springer Verlag, Berlin

Mahendran S, Carrez P, Cordier P (2019) On the glide of [100] dislocation and the origin of 'pencil glide' in Mg_2SiO_4 olivine. Philos Mag 99:2751–2769. https://doi.org/10.1080/14786435.2019.1638530

Mussi A, Nafi M, Demouchy S, Cordier P (2015) On the deformation mechanism of olivine single crystals at lithospheric temperatures: an electron tomography study. Eur J Mineral 27:707–715

Pantleon W (2008) Resolving the geometrically necessary dislocation content by conventional electron backscattering diffraction. Scripta Mater 58:994–997. https://doi.org/10.1016/j.scriptamat.2008.01.050

Poirier JP (1975) On the slip systems of olivine. J Geophys Res 80:4059–4061

Poirier JP (1985) Creep of crystals. High-temperature deformation processes in metals ceramics and minerals. Cambridge University Press

Prior DJ (1999) Problems in determining the misorientation axes, for small angular misorientations, using electron backscatter diffraction in the SEM. J Microsc 195:217–225

Raleigh CB (1968) Mechanisms of plastic deformation of olivine. J Geophys Res 73:5391–5406

Tommasi A, Mainprice D, Canova G, Chastel Y (2000) Viscoplastic self-consistent and equilibrium-based modeling of olivine lattice preferred orientations: implications for the upper mantle seismic anisotropy. J Geophys Res 105:7893–7908

Toriumi M, Karato S (1979) Experimental studies on the recovery process of deformed olivines and the mechanical state of the upper mantle. Tectonophysics 49:79–95

Wallis D, Hansen LN, Britton TB, Wilkinson AJ (2016) Geometrically necessary dislocation densities in olivine obtained using high-angular resolution electron backscatter diffraction. Ultramicroscopy 168:34–45. https://doi.org/10.1016/j.ultramic.2016.06.002

Wallis D, Hansen LN, Britton TB, Wilkinson AJ (2017a) Dislocation interactions in olivine revealed by HR-EBSD. J Geophys Res 122:7659–7678. https://doi.org/10.1002/2017JB014513

Wallis D, Parsons AJ, Hansen LN (2017b) Quantifying geometrically necessary dislocations in quartz using HR-EBSD: application to chessboard subgrain boundaries. J Struct Geol 125:235–247. https://doi.org/10.1016/j.jsg.2017.12.012

Wallis D, Hansen L, Tasaka M, Kumamoto K, Parsons A, Lloyd G, Kohlstedt D, Wilkinson A (2019a) The impact of water on slip system activity in olivine and the formation of bimodal crystallographic preferred orientations. Earth Planet Sci Lett 508:51–61. https://doi.org/10.1016/j.epsl.2018.12.007

Wallis D, Hansen LN, Britton TB, Wilkinson AJ (2019b) High-angular resolution electron backscatter diffraction as a new tool for mapping lattice distortion in geological minerals. J Geophys Res 124:6337–6358. https://doi.org/10.1029/2019JB017867

Wilkinson A, Randman D (2010) Determination of elastic strain fields and geometrically necessary dislocation distributions near nanoindents using electron back scatter diffraction. Phil Mag 90:1159–1177

Wilkinson A, Meaden G, Dingley D (2006) High resolution mapping of strains and rotations using electron backscatter diffraction. Mater Sci Technol 22:1271–1278

Wright SI, Nowell MM, Field DP (2011) A review of strain analysis using electron backscatter diffraction. Microsc Microanal 17:316–329. https://doi.org/10.1017/S1431927611000055

Publisher's Note Springer Nature remains neutral with regard to jurisdictional claims in published maps and institutional affiliations.